Supplementary Materials for

Dense dislocation arrays embedded in grain boundaries for high-performance bulk thermoelectrics

Sang Il Kim,* Kyu Hyoung Lee,* Hyeon A Mun,* Hyun Sik Kim, Sung Woo Hwang, Jong Wook Roh, Dae Jin Yang, Weon Ho Shin, Xiang Shu Li, Young Hee Lee, G. Jeffrey Snyder, Sung Wng Kim*

*Corresponding author.
E-mail: sang.il.kim@samsung.com (S.I.K.); kimsungwng@skku.edu (S.W.K.)

Published 3 April 2015, *Science* **348**, 109 (2015)
DOI: 10.1126/science.aaa4166

This PDF file includes:

Contents

Materials and Methods

Ingot preparation

The $Bi_{0.5}Sb_{1.5}Te_3$ ingots were prepared with a melt process; high-purity (> 99.999%) Bi, Sb, and Te granules were weighed according to the composition $Bi_{0.5}Sb_{1.5}Te_3$ and loaded into a vacuum-sealed quartz tube of 10 mm diameter, and the contents were melted and homogeneously mixed in a rocking furnace for 10 h at 1073 K.

Melt spinning

$Bi_{0.5}Sb_{1.5}Te_3$ bulk ingots were pulverized and mixed with excess Tellurium (25 wt%), then the homogeneously mixed materials were put into a quartz cylinder with 0.3 mm diameter nozzle in melt spinning system. The materials were induction-molten, and were injected under a pressure of 40 kPa Ar onto a Cu wheel rotating with linear speed of 45 m s^{-1} under the Ar atmosphere of 300 mTorr. Thin ribbons (5–10 μm thick, 1.5–2 mm wide, and 5–10 mm long) were obtained by rapid solidification (cooling rate ~10^6 K s^{-1}) using this melt spinning process.

Spark plasma sintering

The melt spun ribbons were pulverized, then compacted using spark plasma sintering (SPS) at 480 ^oC for 3 min under 70 MPa for S-MS and Te-MS materials. During the compacting, the liquidified excess Te was expelled from the graphite die.

Characterization and Measurement

X-ray diffraction (XRD) (D/MAX-2500/PC, Rigaku, Japan) analysis with Cu K_α radiation (λ = 1.5418 Å) was performed on powder and bulk samples. The microstructure was investigated using scanning electron microscopy (SEM) (JSM-7600F, JEOL) and transmission electron microscope (TEM) (JEM-2100F, JEOL). Transport measurements were performed in directions both parallel and perpendicular to the pressing direction. Only the measurements perpendicular to the pressing directions are shown in the main text and used for calculation of zT. The electrical conductivities (σ) and Seebeck coefficients (S) were measured from 300 to 480 K by a four point probe method using a ZEM-3 (ULVAC-RIKO, Japan) with confirming measurements using a custom system (section S7). Hall effect measurements were performed using Physical Property Measurement System (Quantum Design) and confirmed with a custom system (section S7). The thermal conductivity values ($\kappa = \rho_s \times C_p \times \lambda$) were calculated from measurements taken separately. Sample density (ρ_s) was measured by Archimedes method. The thermal diffusivity (λ) was measured by laser-flash method using TC-9000 (ULVAC-RIKO, Japan) and confirmed using Netzsch LFA 457 (section S6). The Dulong-Petit heat capacity (C_p = 124.6 J mol^{-1} K^{-1}) was used and confirmed by measurements at 300 K by the thermal relaxation method using a Physical Property Measurement System (Quantum Design) (section S10).

S1. SEM images of melt spun stoichiometric $Bi_{0.5}Sb_{1.5}Te_3$ (S-MS) and 25 wt% Te excess $Bi_{0.5}Sb_{1.5}Te_3$ (Te-MS) samples.

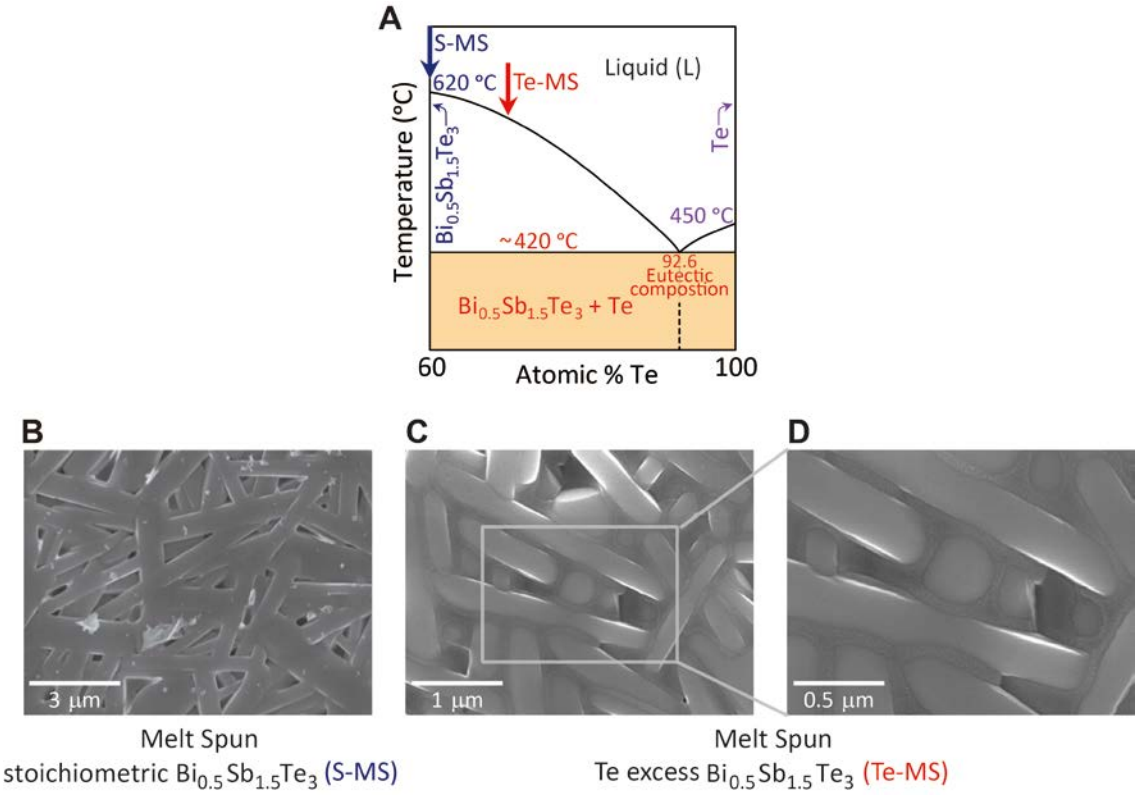

Figure S1. A, Phase diagram of $Bi_{0.5}Sb_{1.5}Te_3$–Te system showing an eutectic composition at 92.6 at% Te. Blue and red arrows indicate the nominal composition of melt spun stoichiometric $Bi_{0.5}Sb_{1.5}Te_3$ (S-MS) and 25 wt% Te excess $Bi_{0.5}Sb_{1.5}Te_3$ (Te-MS) material, respectively (Fig. 3A). **B** and **C**, Scanning electron microscope (SEM) images of melt spun ribbons of S-MS and Te-MS material showing platelets of $Bi_{0.5}Sb_{1.5}Te_3$. **D**, An enlarged view of (C) showing the $Bi_{0.5}Sb_{1.5}Te_3$ platelets surrounded by the eutectic phase of $Bi_{0.5}Sb_{1.5}Te_3$–Te mixture, in which the $Bi_{0.5}Sb_{1.5}Te_3$ particles (white spots) have the size of 10–20 nm (Fig. 3B).

S2. Structural characterization of melt spun Te-MS ribbons with Te excess (25 wt% Te excess $Bi_{0.5}Sb_{1.5}Te_3$) and compacted Te-MS samples.

A

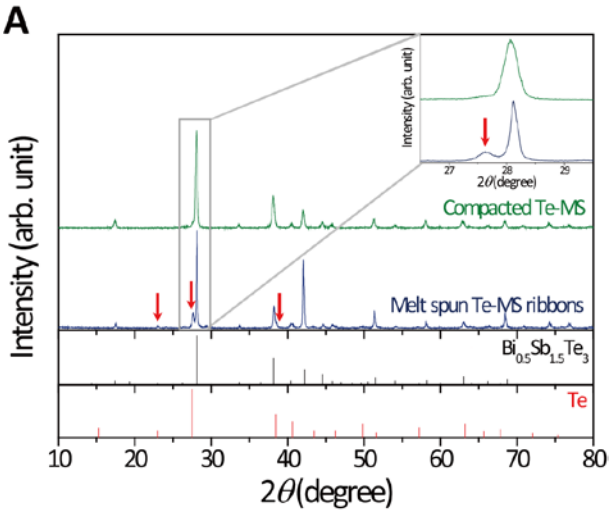

B

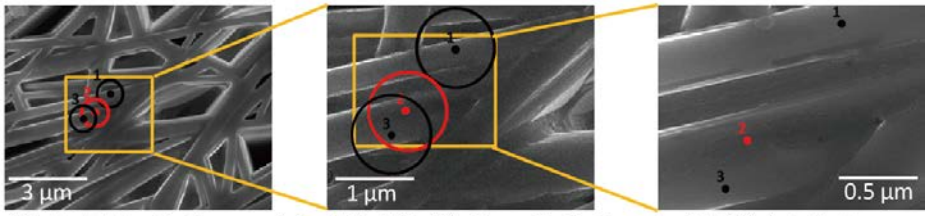

※ dashed circle : detection range (~1 μm), Black (#1, #3) : Primary $Bi_{0.5}Sb_{1.5}Te_3$ grains, Red (#2) : Eutectic phases

Element	at%		
	#1	#2	#3
Bi	8.27	5.99	7.60
Sb	22.54	18.67	22.21
Te	69.19	75.33	70.19

C

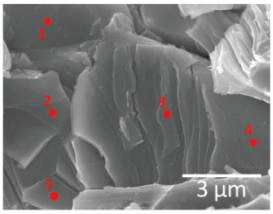

Element	at%				
	#1	#2	#3	#4	#5
Bi	10.02	9.89	10.09	10.01	9.97
Sb	30.29	30.12	29.88	29.90	29.99
Te	59.69	59.99	60.03	60.09	60.04

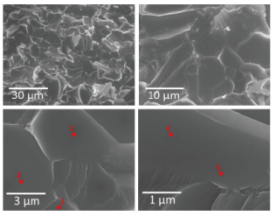

Element	at%				
	#1	#2	#3	#4	#5
Bi	10.06	9.99	9.98	10.04	10.02
Sb	30.04	30.03	29.89	29.99	29.68
Te	59.90	59.98	60.14	59.97	60.30

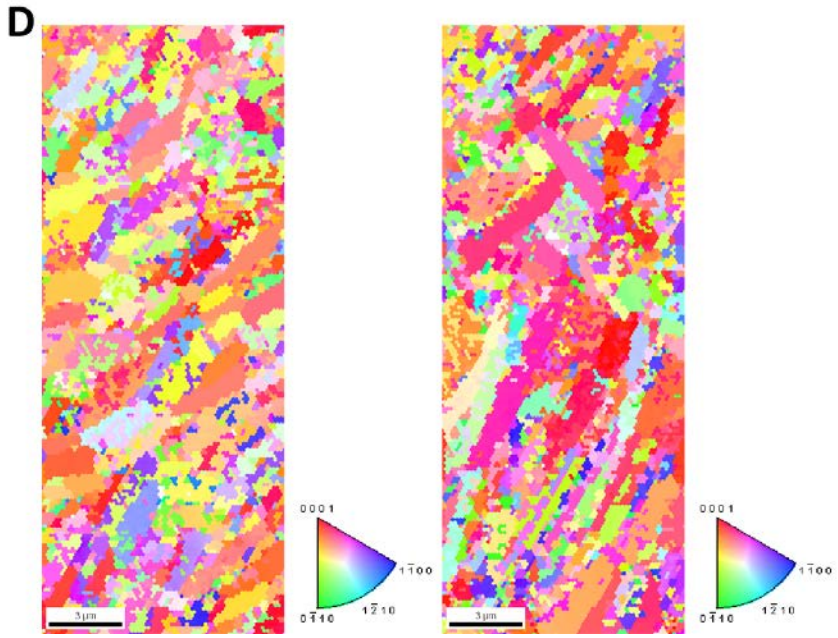

Figure S2. A, X-ray diffraction patterns of melt spun ribbons with Te excess samples. The peak indicated by red arrows is of Te elements and the others are well matched with the diffraction pattern of $Bi_{0.5}Sb_{1.5}Te_3$ alloy, indicating melt spun ribbons with Te excess samples still have an excess Te elements. **B**, SEM-EDS measurements on melt spun ribbons of Te-MS samples. The distinct difference in the amount of Te elements between primary $Bi_{0.5}Sb_{1.5}Te_3$ grains (#1 and #3) and eutectic phases (#2) was clearly observed, indicating excess Te elements exist between primary $Bi_{0.5}Sb_{1.5}Te_3$ grains. It was hard to independently analyze each $Bi_{0.5}Sb_{1.5}Te_3$ grain and eutectic phase due to the limit of detecting range (~ 1 μm) in energy dispersion spectroscopy of scanning electron microscopy. **C**, SEM-EDS measurements on compacted Te-MS samples. The results clearly showed no distinct region of excess Te elements and Te-rich $Bi_{0.5}Sb_{1.5}Te_3$ composition. **D**, Electron backscatter diffraction (EBSD) image showed a nearly random crystallographic orientation of polycrystalline compacted Te-MS samples with an average grain size of ~ 280 nm.

Table S1. Inductively coupled plasma mass spectrometry (ICP-MS) results for compacted S-MS and Te-MS samples. The results indicate the compacted Te-MS samples are stoichiometric $Bi_{0.5}Sb_{1.5}Te_3$ alloys without excess Te elements.

Materials	Mole ratio (%)		
	Sb	Te	Bi
$Bi_{0.5}Sb_{1.5}Te_3$ (standard)	28.9	61.1	10.0
S-MS	29.6	60.1	10.3
Te-MS #1	29.4	60.7	9.9
Te-MS #2	29.4	60.4	10.2
Te-MS #3	29.7	60.2	10.1
$Bi_{0.5}Sb_{1.5}Te_3$ (Nominal)	30	60	10
25 wt% Te excess $Bi_{0.5}Sb_{1.5}Te_3$ (Nominal)	23.8	68.3	7.9

S3. Expelled excess Te along with $Bi_{0.5}Sb_{1.5}Te_3$ nano-particles from graphite die.

Figure S3 shows the pictures after transient liquid flow compacting process (using spark plasma sintering) for Te-MS sample, where the solidified eutectic phases (mixture of solidified excess Te and $Bi_{0.5}Sb_{1.5}Te_3$ nano-particles) are shown on the top of graphite die. Excess Te was expelled as a liquid along with solid $Bi_{0.5}Sb_{1.5}Te_3$ nano-particles (that is, eutectic phases) during the compaction at 480 ^{o}C. Figure S4 shows the X-ray diffraction patterns of expelled excess Te along with $Bi_{0.5}Sb_{1.5}Te_3$ nano-particles from graphite die. As a result, the compacted Te-MS samples were single phase BST alloys with stoichiometric composition of $Bi_{0.5}Sb_{1.5}Te_3$ alloy, as confirmed from XRD and ICP measurements (Fig. S2A and Table S1). Furthermore, the SEM-EDS showed no distinct region of excess Te elements and Te-rich $Bi_{0.5}Sb_{1.5}Te_3$ composition (Fig. S2C).

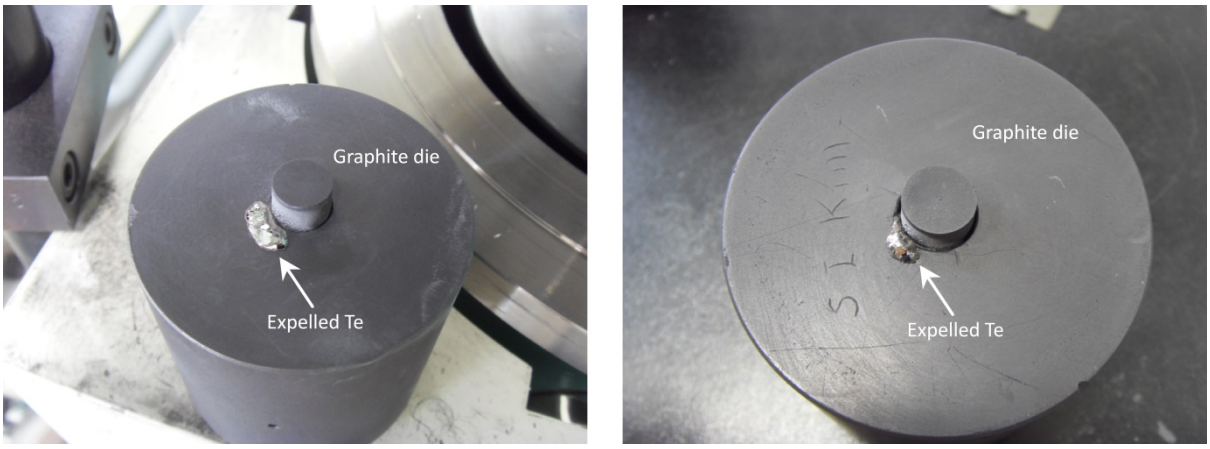

Figure S3. Pictures after transient liquid flow compacting process (spark plasma sintering) for 25 wt% Te excess $Bi_{0.5}Sb_{1.5}Te_3$ (Te-MS) material.

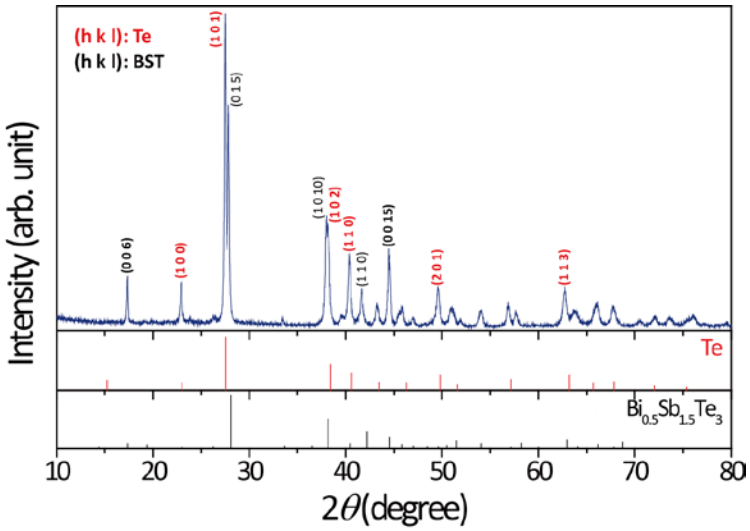

Figure S4. Powder X-ray diffraction patterns of expelled excess Te along with $Bi_{0.5}Sb_{1.5}Te_3$ nano-particles (eutectic phases).

S4. Samples for thermoelectric transport properties measurements

The inner diameter of graphite die was about 10.4 mm. We fabricated the disk-shaped samples of 10.4 mm in diameter and 12.5–13 mm in thickness as shown in Fig. S5A. The acquired samples were ground into disk of 10 mm in diameter and 12 mm in thickness as shown in Fig. S5B. In order to measure the thermoelectric properties in both directions parallel and perpendicular to the press direction, disks of 10 mm diameter and 1.5 mm thickness and bars of about 3 mm × 1 mm × 9 mm were made from both directions by grinding of the 4 samples shown in Fig. S5C. Disk for the thermal diffusivity measurement along the perpendicular to the press direction was made from square-shaped sample (10 mm × 10 mm × 1.5 mm).

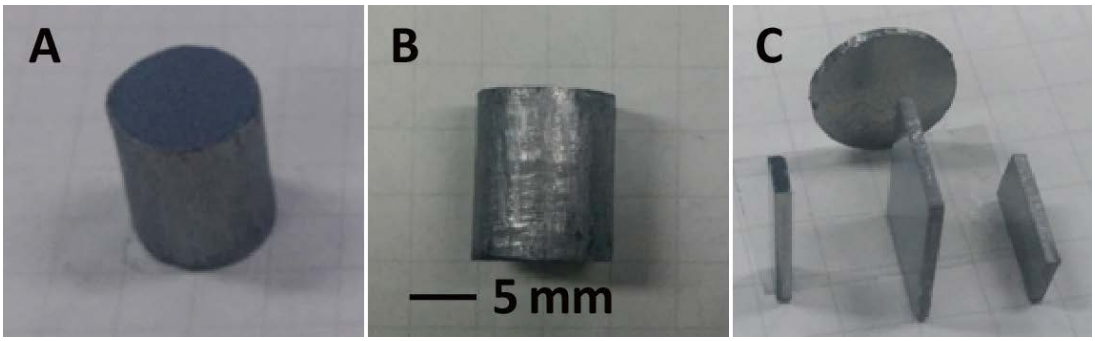

Figure S5. A and **B**, Pictures of the final product after transient liquid flow compacting process (spark plasma sintering). **C**, Pictures after cutting the compacted samples.

S5. Anisotropic crystal structure and thermoelectric transport properties.

Figure S6 shows the X-ray diffraction patterns of both the planes parallel (||) and perpendicular (⊥) to the press directions for BM, S-MS, and Te-MS samples. The texture fraction of the {0 0 *l*} planes was calculated from X-ray diffraction patterns scanned from $2\theta = 10^{o}$ to 60^{o} by Lotgering method. The degree of orientation (*f*) is defined as $f_{00l} = (p_{00l} - p_0)/(1 - p_0)$, where $p_{00l} = \Sigma I_{00l}/\Sigma I_{hkl}$ and $p_0 = \Sigma I^0_{00l}/\Sigma I^0_{hkl}$ with I_{hkl} and I^0_{hkl} being the intensities of (*h k l*) peaks for the textured and randomly oriented sample, respectively. The f_{00l} values for BM, S-MS, and Te-MS samples in the perpendicular direction are 0.089 (BM), 0.095 (S-MS), and 0.108 (Te-MS), while those for the plane parallel to the press direction are 0.076 (BM), 0.068 (S-MS), and 0.061 (Te-MS). All samples showed the anisotropy in crystal structure, but the degree of anisotropic orientation was not much significant in all samples.

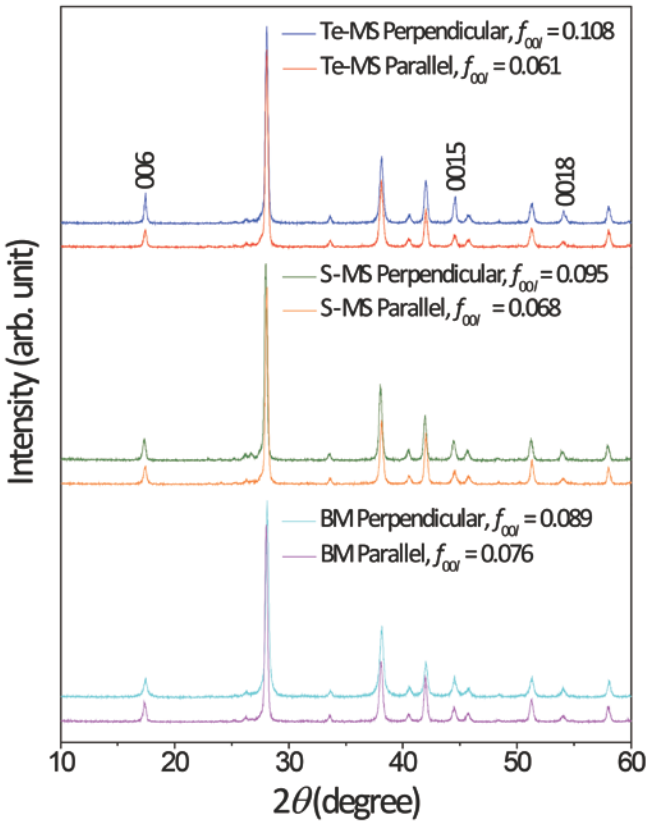

Figure S6. X-ray diffraction patterns of both the planes parallel (||) and perpendicular (⊥) to the press directions for BM, S-MS, and Te-MS samples, showing the anisotropic properties in all samples.

We measured all thermoelectric transport properties (electrical conductivity (σ), Seebeck coefficient (S), and thermal conductivity (κ)) both in parallel and perpendicular to the press directions. In Fig. S7, we showed the temperature dependence of σ, S, power factor (PF), κ and zT of the BM, S-MS, and Te-MS samples in both the directions perpendicular ($\sigma_{\perp}$, $S_{\perp}$, $PF_{\perp}$, $\kappa_{tot\perp}$, $\kappa_{lat\perp}$, and $zT_{\perp}$) and parallel ($\sigma_{\parallel}$, $S_{\parallel}$, $PF_{\parallel}$, $\kappa_{tot\parallel}$, $\kappa_{lat\parallel}$, and $zT_{\parallel}$) to the press direction. For Te-MS sample, the $\sigma_{\perp}$ is about 16.5% higher than $\sigma_{\parallel}$ for the whole temperature range, which clearly shows that there is a little *ab* plane orientation along the perpendicular to the press direction, while $\sigma_{\perp}$ values of BM (~ 6.7%) and S-MS (~ 11.4%) samples are slightly higher than $\sigma_{\parallel}$, consistent with the results of X-ray diffraction data (Fig. S7A). On the other hand, S values for BM, S-MS, and Te-MS samples are very similar in both directions (Fig. S7B). The $\kappa_{tot\parallel}$ value of Te-MS sample is ~ 6.1% lower (0.62 W m^{-1} K^{-1} at 320 K with a lattice contribution of 0.34 W m^{-1} K^{-1}) than $\kappa_{tot\perp}$ (0.66 W m^{-1} K^{-1} at 320 K with a lattice contribution of 0.33 W m^{-1} K^{-1}) mainly due to the reduction in electronic contribution by decrease in σ (Figs. S7D and S7E). The maximum $zT_{\perp}$ is about 1.86 at 320 K, which is about a 11% higher than $zT_{\parallel}$ (~ 1.67 at 320 K) as shown in Fig. S7F.

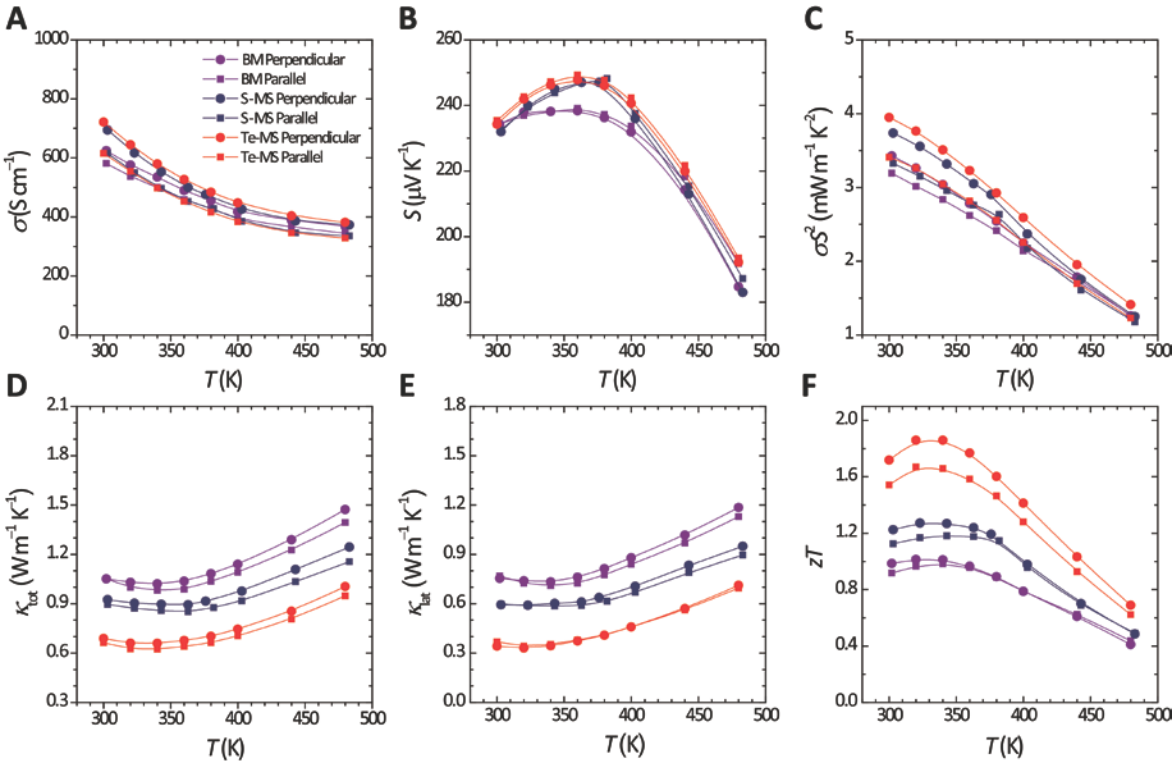

Figure S7. Anisotropic thermoelectric properties of BM, S-MS and Te-MS samples. **A**, Temperature dependence of electrical conductivity (σ). **B**, Temperature dependence of Seebeck coefficient (S). **C**, Temperature dependence of power factor (σS^2). **D**, Temperature dependence of total thermal conductivity (κ_{tot}). **E**, Temperature dependence of lattice thermal conductivity (κ_{lat}). **F**, Temperature dependence of dimensionless figure of merit (zT).

S6. Thermal diffusivity of Te-MS samples

The values of thermal diffusivity for 4 different Te-MS samples were cross-checked by using the instrument LFA-457 of Netzsch. There is no significant difference between the values of thermal diffusivity measured with TC-9000 (ULVAC-RIKO) and LFA as shown in Fig. S8A. Furthermore, Figure S8B showed the comparison of the values in Fig. S8A and the values of 30 Te-MS samples (measured with TC-9000) in Fig. S9D. All values of Fig. S8A are in the range of values of 30 Te-MS samples

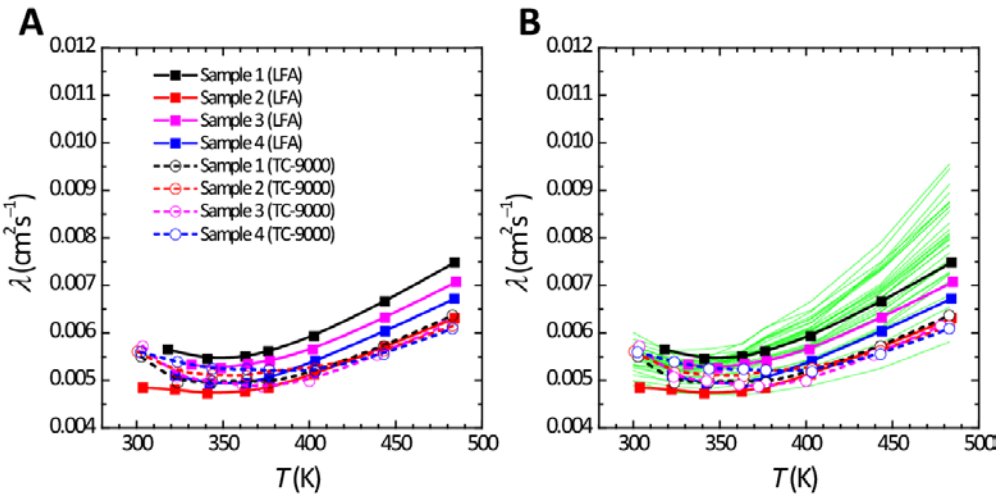

Figure S8. Thermal diffusivity of Te-MS samples. A, Comparison of the values measured with TC-9000 (ULVAC-RIKO) and LFA (Netzsch) for 4 Te-MS samples. **B**, Comparison of the values measured by LFA (Netzsch) for 4 Te-MS samples with the values measured by TC-9000 (ULVAC-RIKO) for 30 Te-MS samples of Fig. S9D.

S7. Reproducibility of high-performance thermoelectric properties of Te-MS samples

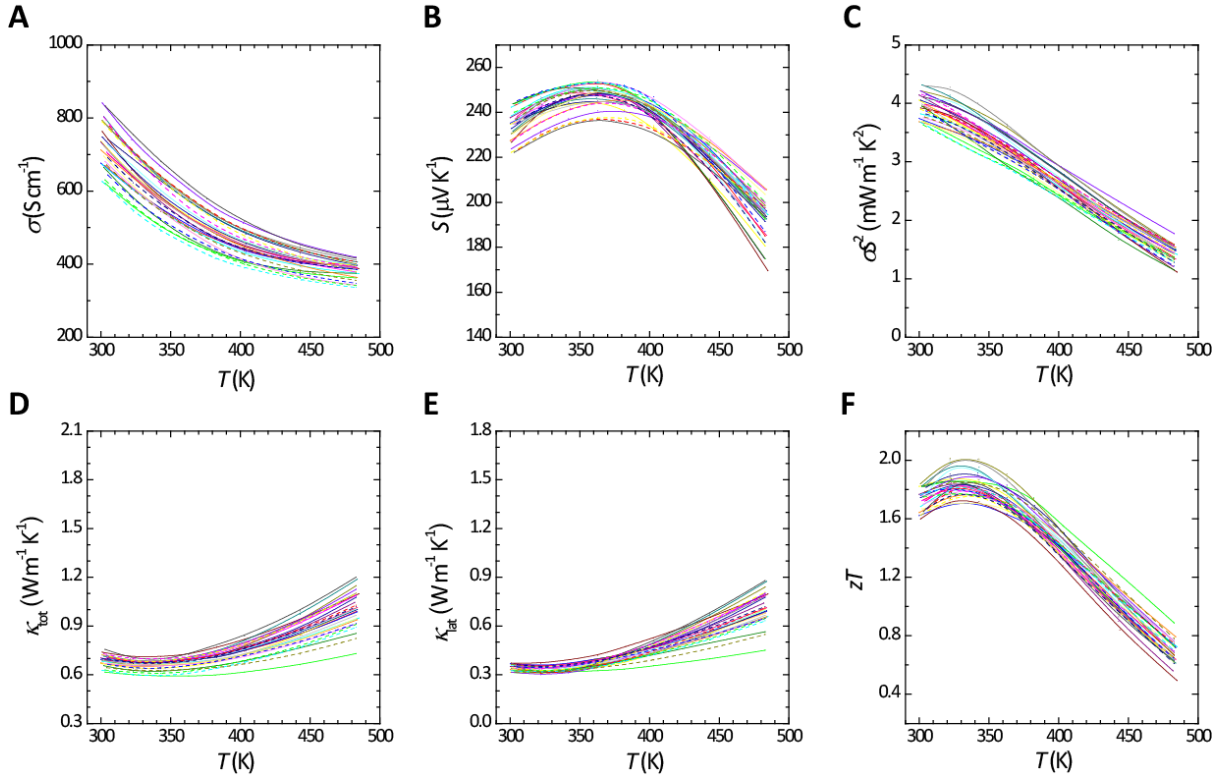

Figure S9. Temperature dependence of thermoelectric properties for 30 Te-MS samples with dislocation arrays embedded in grain boundaries. A, Electrical conductivity (σ). **B**, Seebeck coefficient (S). **C**, Power factor (σS^2). **D**, Total thermal conductivity (κ_{tot}). **E**, Lattice thermal conductivity (κ_{lat}). **F**, Dimensionless figure of merit (zT).

Table S2. Cross-check of carrier concentration (n) and mobility (μ) of compacted Te-MS samples. The results of the table were obtained at Caltech are similar to those of the compacted Te-MS samples.

	n (10^{19} cm^{-3})	μ (cm^2 V^{-1} S^{-1})
#1	1.96 ± 0.03	275 ± 5
#2	1.75 ± 0.05	309 ± 2
#3	1.60 ± 0.01	321 ± 4

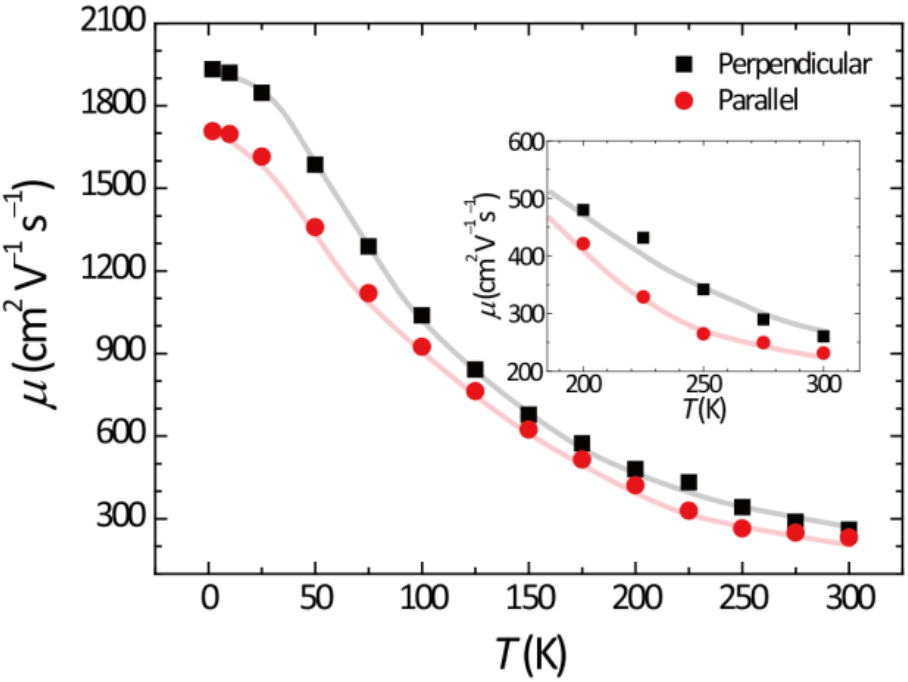

Figure S10. Anisotropic mobility of Te-MS sample.

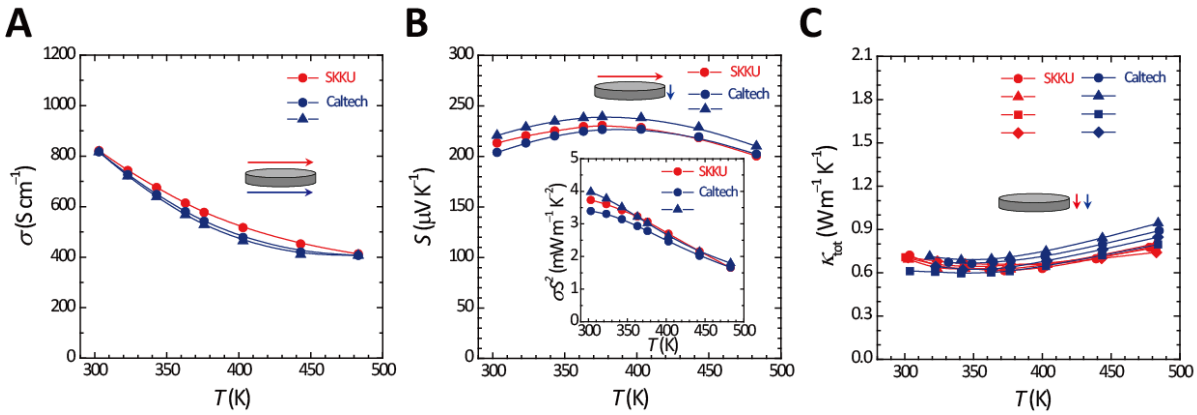

Figure S11. Cross-check of thermoelectric transport properties for Te-MS samples. **A**, Temperature dependence of electrical conductivity (σ). **B**, Temperature dependence of Seebeck coefficient (S). Inset is the power factor (σS^2). **C**, Temperature dependence of total thermal conductivity (κ_{tot}). Arrows indicate the direction of measurements. The measurements at Caltech are described in elsewhere (*35*, *36*).

S8. Compatibility factor of Te-MS sample

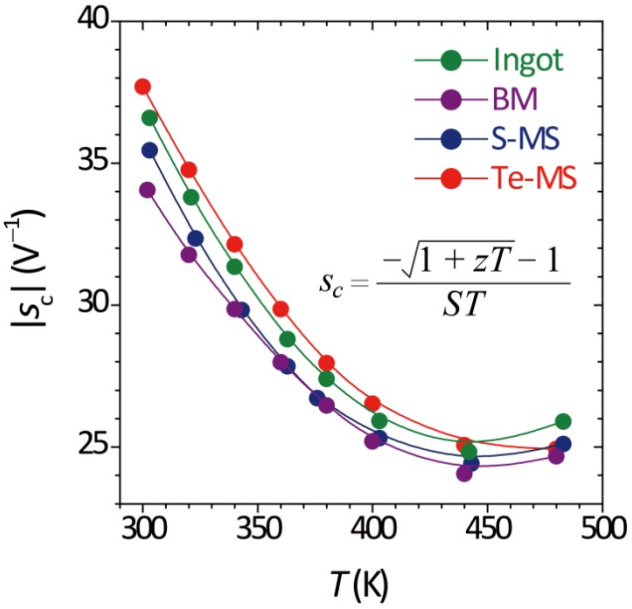

Figure S12. Comparison of compatibility factors of $Bi_{0.5}Sb_{1.5}Te_3$ between different fabrication methods. The compatibility factor (s_c) was calculated with the equation of $s_c = \frac{-\sqrt{1+zT}-1}{ST}$ (*37*). The compatibility factor for Te-MS sample showed a similar value as those of other samples in the whole measured temperature ranges.

S9. TEM images of dislocation arrays embedded in grain boundaries for Te-MS samples.

Figure S13 shows the TEM images observed at slightly tilted zone axis from Fig. 4B of the manuscript. Figure S14 shows the TEM images observed by tilting the TEM zone axis of boxed region B and E in Fig. S13A. Figure S15A shows the classical Moiré fringe. From the fast Fourier-transformed (FFT) image of Fig. S15A as shown in Fig. S15B, it is clearly shown that the (1 1 0) atomic planes of the right grain and the (1 1 $\bar{6}$) atomic planes of the left grain match, forming the misfit dislocations as indicated with the red symbols. The misfit between the two planes is ~ 0.05 Å, which is the 2.8% of *d*-spacing. The misfit of 2.8% is energetically favorable to form misfit dislocations. And, the misfit compensates the misfit spacing of ~ 2.5 nm, as shown in Fig. S15B. This spacing is identical to the periodic spacing of the Moiré fringes of Fig. S15A. Figure S16C shows the high resolution TEM image of dislocation arrays (encircled in white) embedded in grain boundary of Fig. 4H. Figures S17 and S18 show other TEM images of dislocation arrays embedded in grain boundaries for compacted Te-MS samples.

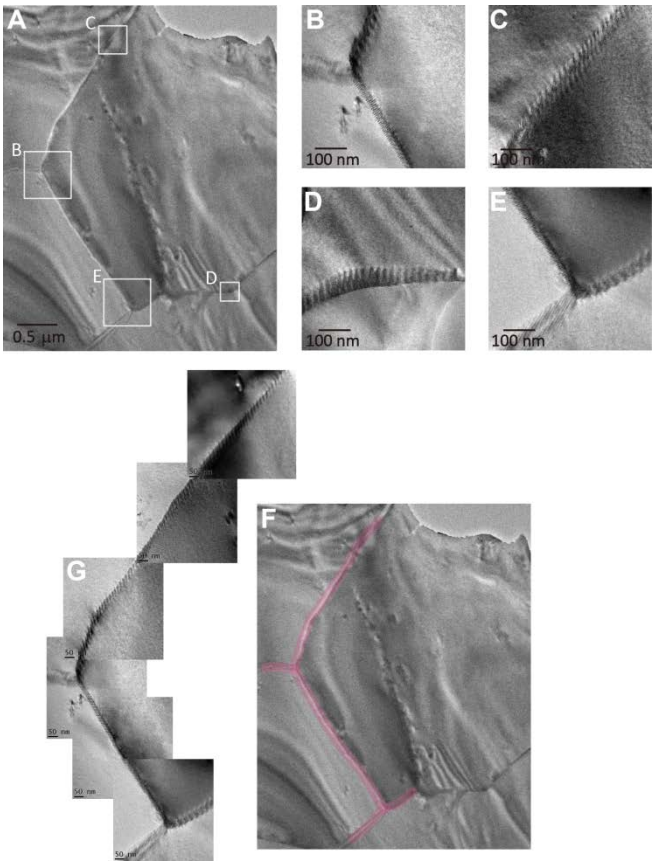

Figure S13. Dislocation arrays embedded in grain boundaries. A, TEM images observed at slightly tilted zone axis from Fig. 4B. **B–E**, Enlarged views of boxed regions in A. **F**–**G,** Comprised TEM images of the pink-colored grain boundary area of F.

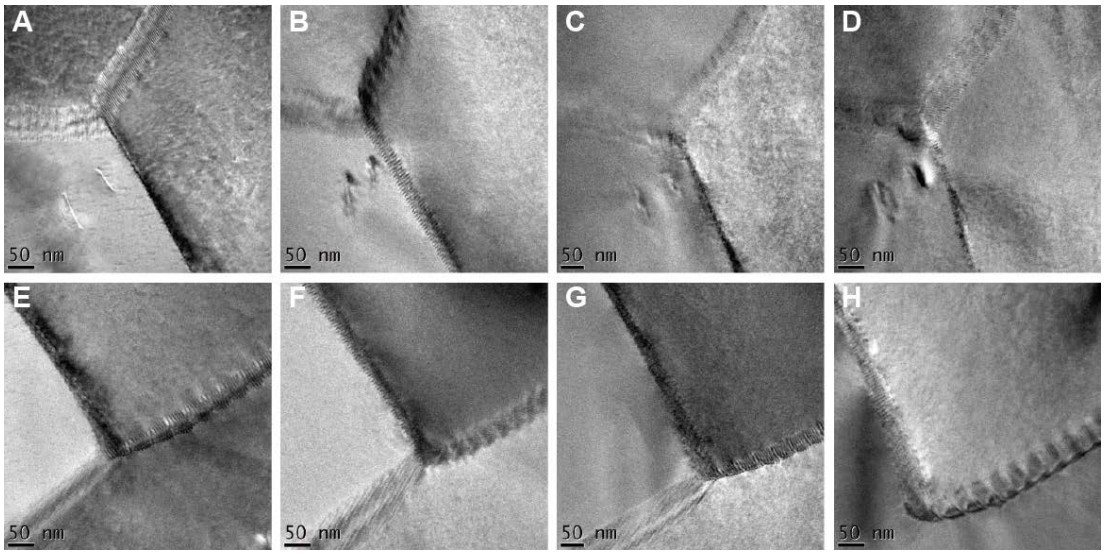

Figure S14. Grain boundary images by tilting the TEM zone axis. Images of central grain boundary change by tilting the TEM zone axis, showing the appearance and disappearance of Moiré fringes.

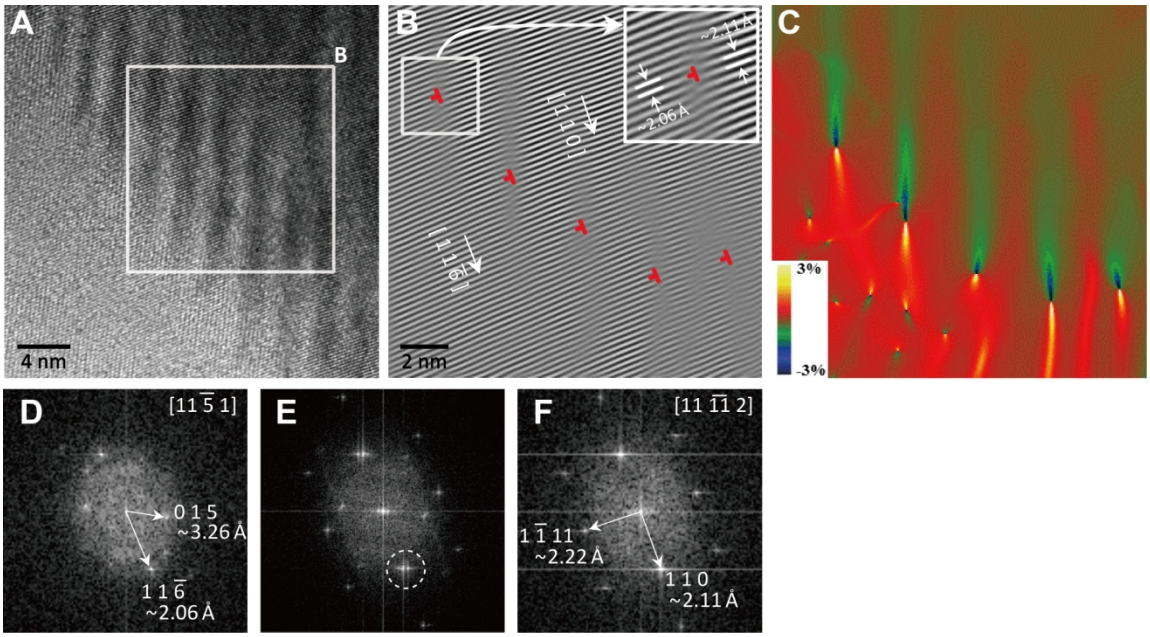

Figure S15. Dislocation arrays embedded in grain boundaries. A, High resolution TEM image of a grain boundary. **B**, Inverse FFT (IFFT) image with (1 1 $\bar{6}$) and (1 1 0) planes for the left and right grains, respectively, of boxed region in A. **C**, Strain mapping of B, showing the dislocation cores with the high intensity. Inset is the enlarged view of boxed region in B. **D**–**F**, FFT images of left, center and right grains, respectively.

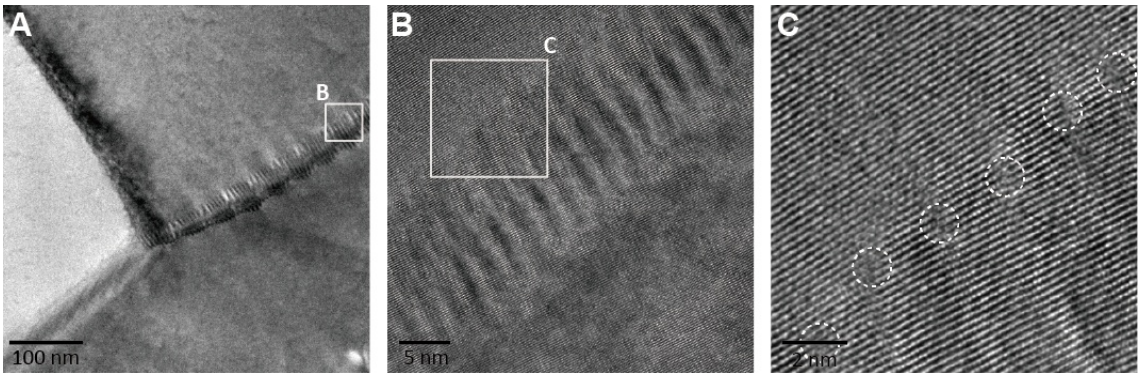

Figure S16. Dislocation arrays embedded in grain boundaries. A, High resolution TEM image of a grain boundary of Fig. 4H in main text. **B**, Enlarged view of boxed region in A. **C**, Enlarged view of boxed region in B, showing some dislocations encircled in white.

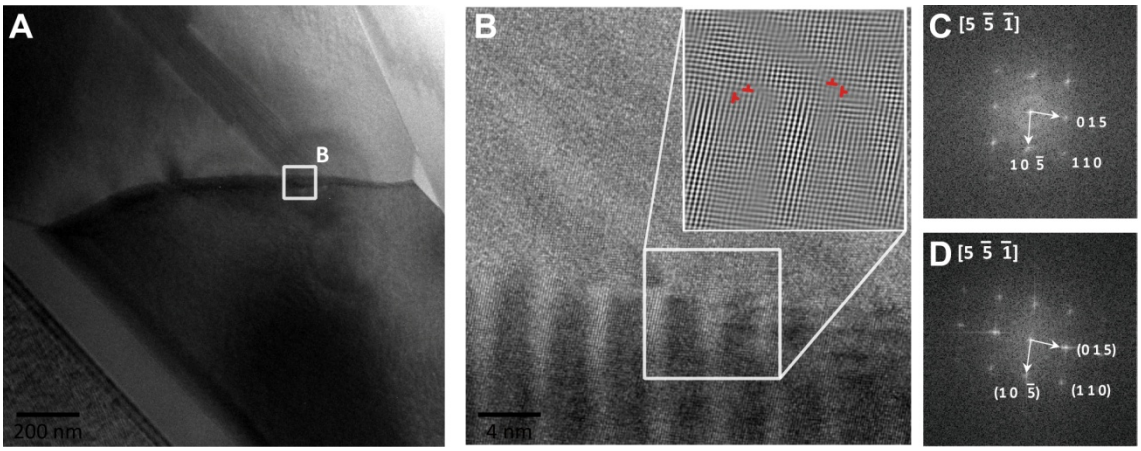

Figure S17. Dislocation arrays embedded in grain boundaries. A, Low-magnification TEM image of a grain boundary. **B**, High resolution TEM image of a grain boundary. Inset, IFFT image of boxed region. **C** and **D**, FFT images of top and bottom grains in **B**. The FFT images revealed the 3^{o} misorientation between two adjacent grains. The arrays of alternating edge dislocation pairs are quite similar to the periodic dislocations observed in low angle (7^{o}) grain boundary of Bi_2Se_3 thin film (*38*).

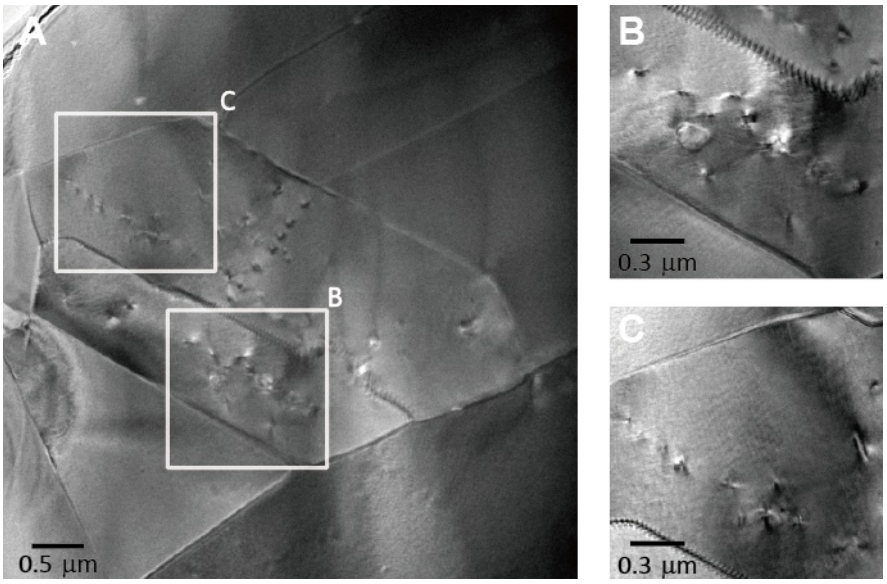

Figure S18. Low-magnification TEM images of dislocation arrays embedded in grain boundaries. Images show a Moiré pattern (~ 90 nm wide) at central grain boundary and the other grain boundaries without Moiré pattern have an width up to ~ 60 nm that is quite wide compared to the few nanometer width as observed in the S-MS material (Fig. 4A).

S10. Energy dispersion spectroscopy measurement around grain boundaries in compacted Te-MS sample.

Figure S19 shows the STEM-EDS elemental-mapping image of Te for the similar image as Fig. S13C, indicating no presence of remaining Te at grain boundaries and no distinct Te increase in the compositions of adjacent $Bi_{0.5}Sb_{1.5}Te_3$ grains.

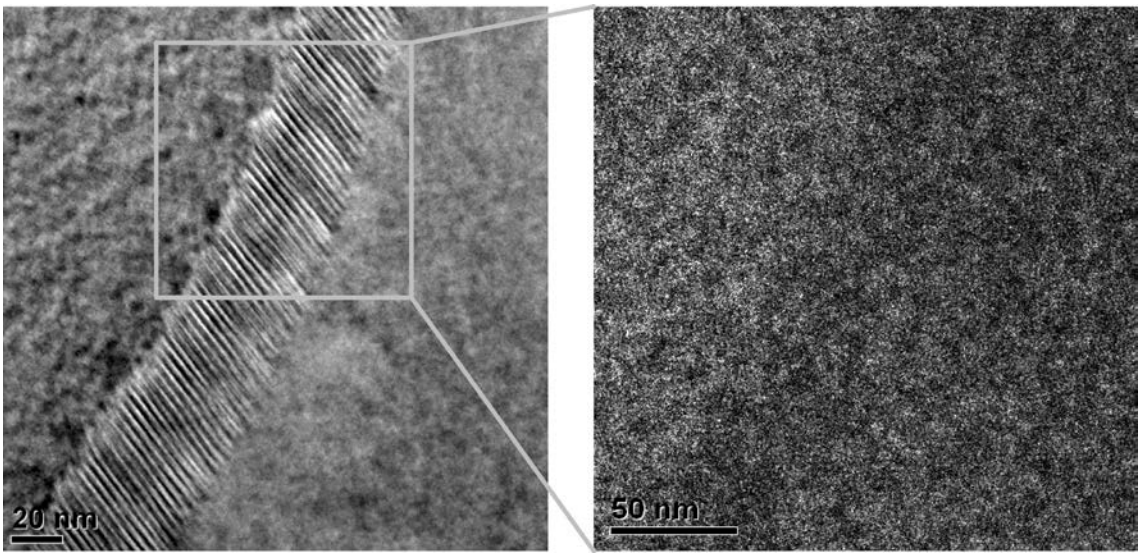

Figure S19. STEM-EDS elemental-mapping image of Te for compacted Te-MS sample.

S11. Heat capacity (C_p) of $Bi_{0.5}Sb_{1.5}Te_3$ samples

We measured the heat capacity of BM, S-MS and Te-MS materials for the calculation of thermal conductivity and used the reference data for Ingot material (124.6 J mol^{-1} K^{-1}) (*38*). Figure S20 shows the temperature dependence of BM, S-MS and Te-MS materials, showing a similar value (BM: 124.6 J mol^{-1} K^{-1}, S-MS: 124.8 J mol^{-1} K^{-1}, Te-MS: 124.6 J mol^{-1} K^{-1}) at 300 K. The densities (ρ_s) of Ingot (6.88 g cm^{-3}), BM (6.78 g cm^{-3}), S-MS (6.77 g cm^{-3}) and Te-MS (6.76±0.03 g cm^{-3}) materials measured by Archimedes method were used for thermal conductivity calculation.

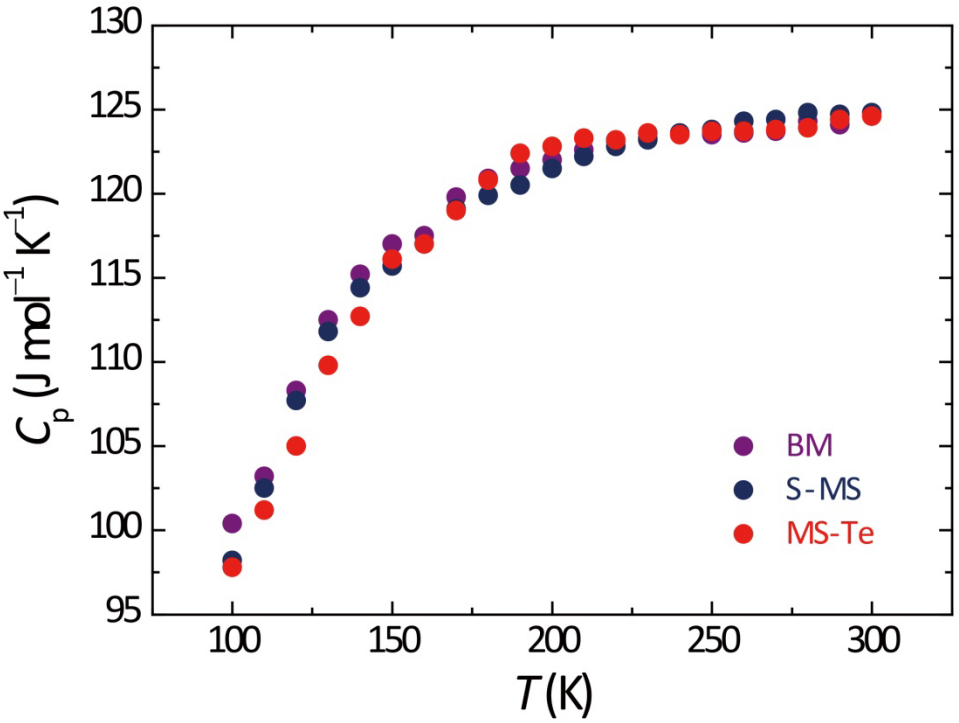

Figure S20. The temperature dependence of heat capacity (C_p) for $Bi_{0.5}Sb_{1.5}Te_3$ samples (BM, S-MS and Te-MS) measured in the range from 100 K to 300 K by thermal relaxation method using Physical Property Measurement System (Quantum Design). The heat capacity value of 124.6 J mol^{-1} K^{-1} was used for Ingot material (*39*).

S12. Calculation of Lorenz number

The value of κ_{lat} was calculated by subtraction of κ_{ele} form κ_{tot}, which was estimated using the Wiedemann-Franz law ($\kappa_{ele} = L_0 \times T \times \sigma$), where L_0, T, and σ denote the Lorenz number, absolute temperature and electrical conductivity. The Lorenz number, L_0 was obtained using following equation:

$$L_0 = \left(\frac{k_B}{e}\right)^2 \left(\frac{(r+7/2)F_{r+5/2}(\eta)}{(r+3/2)F_{r+1/2}(\eta)} - \left[\frac{(r+5/2)F_{r+3/2}(\eta)}{(r+3/2)F_{r+1/2}(\eta)}\right]^2 \right),$$

where k_B is the Boltzmann constant, e is the electron charge, r is the scattering parameter, $F_n(\eta)$ is the n-th order Fermi integral, $F_n(\eta) = \int_0^\infty \frac{x^n}{1+e^{x-\eta}} dx$, and η is the reduced Fermi energy, respectively. For the L_0 calculation, η was calculated from the following relationship using the measured Seebeck coefficient (S):

$$S = \pm \frac{k_B}{e} \left(\frac{(r+5/2)F_{r+3/2}(\eta)}{(r+3/2)F_{r+1/2}(\eta)} - \eta \right),$$

and r was derived from the temperature dependence of the carrier mobility. The values of L_0 at 300 K were found 1.603×10^{-8}, 1.574×10^{-8}, 1.614×10^{-8} $V^2 K^{-2}$ for BM, S-MS, Te-MS materials, respectively.

S13. Calculation of ΔT_{max} of modules

Two thermoelectric modules of the same size (127 couples) were fabricated, where the only difference between them lied in the materials used for p-type legs. For one module, the ingot was utilized for the p-type legs, while the Te-MS was used in another one.

Maximum values for coefficient of performance (COP_{max}) were taken at different ΔT in COP versus input current. The values of COP_{max} for two modules were plotted as filled circles in Fig. 1E. By assuming asymmetric thermal contact resistivity of the modules, following equation was derived from Min's equation (*40*, *41*) for a module with symmetric thermal contacts.

$$\mathrm{COP_{max}} = \left(\frac{1}{1+\frac{rl_c}{l}}\right)\left[\frac{T_c}{T_h-T_c}\frac{\left(1+Z\frac{T_h+T_c}{2}\right)^{1/2}-\frac{T_h}{T_c}}{\left(1+Z\frac{T_h+T_c}{2}\right)^{1/2}+1}\right] \quad (1)$$

where l_c and l are the length as shown in Fig. S21 and r corresponds to thermal conductivity of thermoelements divided by that of the contact layers (ceramic plate + conducting strip). Variables r and Z were adjusted to fit calculated COP_{max} (lines in Fig. 1E) to experimental COP_{max} (filled circles in Fig. 1E) data. The ΔT_{max} of a module was obtained from a ΔT value when COP_{max} becomes zero.

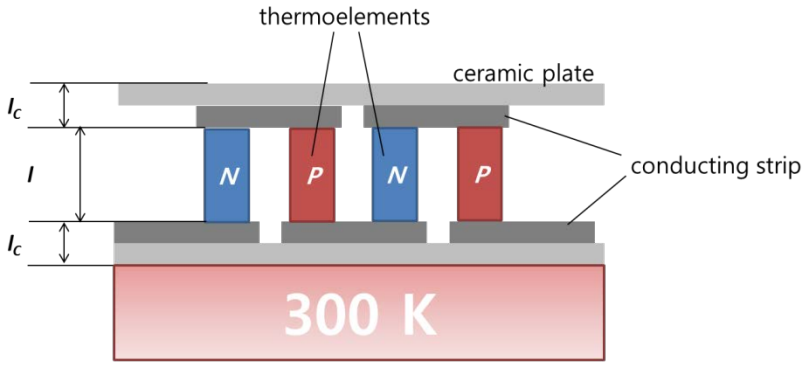

Figure S21. Schematic illustration of thermoelectric module.

S14. Model of lattice thermal conductivity

Lattice thermal conductivities (κ_{lat}) of BM, S-MS and Te-MS were explained using the Debye-Callaway model (*26, 29*). We followed the Bessas' model (*42*) who found the acoustic phonons are the dominant contribution to lattice thermal conductivity. In the Debye-Callaway model, the total phonon relaxation time (τ_{tot}) is a reciprocal sum of the relaxation times of the pertinent scattering mechanisms. Once τ_{tot} is obtained, it is used to calculate the lattice thermal conductivity from eqn. 1.

$$\kappa_{\mathrm{lat}} = \frac{k_{\mathrm{B}}}{2\pi^2 v}\left(\frac{k_{\mathrm{B}}T}{\hbar}\right)\int_0^{\theta_{\mathrm{a}}/T} \tau_{\mathrm{tot}}(x)\frac{x^4 e^x}{(e^x-1)^2}\,dx \qquad (1)$$

The three dominant scattering mechanisms relevant to all $(Bi_{0.25}Sb_{0.75})_2Te_3$ polycrystalline samples are Umklapp phonon-phonon scattering, point-defect scattering and boundary scattering. The relaxation time associated with Umklapp phonon-phonon scattering (τ_U) (*9, 27, 28*) is calculated from eqn. 2 (see Table S4).

$$\tau_{\mathrm{U}}{}^{-1} = A_{\mathrm{N}}\frac{2}{(6\pi^2)^{1/3}}\frac{k_{\mathrm{B}}\bar{V}^{1/3}\gamma^2\omega^2 T}{\bar{M}v^3} \qquad (2)$$

The impact of normal phonon-phonon scattering (τ_N) in the calculation of κ_{lat} can be expressed in terms of τ_U (*29*) which leads to an additional factor (A_N = 2.6 see Table S3). This factor is determined by fitting experimental literature data from Stordeur (*43*) on well characterized crystalline material.

The relaxation time associated with point-defect scattering (τ_{PD}) (*12, 30, 31*) is given by eqn. 3 (see Table S4).

$$\tau_{\mathrm{PD}}{}^{-1} = \frac{Vw^4}{4\pi v^3}\Gamma \qquad (3)$$

The mass and lattice constant contrasts between Bi and Sb in $(Bi_{0.25}Sb_{0.75})_2Te_3$ are the sources of point-defect scattering, and they are described in Γ (*12, 30*). The value of Γ = 0.145 (in Table S4) for $(Bi_{0.25}Sb_{0.75})_2Te_3$ is determined by fitting experimental literature data from Stordeur (*43*).

The relaxation time associated with boundary scattering (τ_B) (*9, 31, 44*) is given by eqn. 4 (see Table S4).

$$\tau_{\mathrm{B}}{}^{-1} = \frac{v}{d} \qquad (4)$$

We use the observed average grain size of 50 μm for BM and 300 nm for S-MS and Te-MS samples to calculate τ_B (τ_U and τ_{PD} were kept unchanged since all these samples have the same composition - see Table 3).

Finally, to model the κ_{lat} of Te-MS, introduction of additional relaxation times associated with dislocations was necessary. The scattering mechanism from dislocations can be divided into scattering from dislocation strain and that from dislocation cores; hence they have separate phonon relaxation times τ_{DC} (*10, 29, 46, 47*) and τ_{DS} (*10, 29, 45, 46*), respectively (see eqn. 5–6). Because an array of dislocations at grain boundaries can be physically treated as a collection of single dislocations inside a grain (*47*), we include τ_{DC} and τ_{DS} to calculate the τ_{tot} of Te-MS.

$$\tau_{DC}^{-1} = N_D \frac{\overline{V}^{4/3}}{v^2} \omega^3 \quad (5)$$

$$\tau_{DS}^{-1} = 0.6 \times B_D^2 N_D (\gamma + \gamma_1)^2 \omega \left[\frac{1}{2} + \frac{1}{24} \left(\frac{1-2r}{1-r} \right)^2 \left\{ 1 + \sqrt{2} \left(\frac{v_L}{v_T} \right)^2 \right\}^2 \right] \quad (6)$$

N_D, B_D, γ, γ_1, r, ν_L, ν_T are dislocation density, effective Burger's vector, Grüneisen parameter, change in Grüneisen parameter, Poisson's ratio, longitudinal phonon velocity and transverse phonon velocity, respectively (see Table S4). The scatter of dislocation cores only requires N_D, $\overline{V}$ and ν with no fitting parameters (see eqn. 5). It is important to note that different values of constant (A) in front of B_D^2 in τ_{DS}^{-1} have been used by Klemens. In 1955, Klemens began with A=0.06 as the constant of proportionality (*10*). Three years later, he hinted that the constant 0.06 should be multiplied by 16 (*45*) and used $0.96 B_D^2 \tau_{DS}^{-1}$ equation to model thermal resistivity in experiments with copper alloys (*48, 49*). His latest book presents the equation of $1.1 B_D^2 \tau_{DS}^{-1}$ (*10*). Another factor of 0.55 is needed to account for arrays of dislocations oriented in random direction (*46*), resulting in the 0.6 used here.

Klemens also pointed out that for an alloy with dislocations, the concentration of the solute atoms could be modulated by the strain fields around the dislocations (*10, 45*). This can reinforce or oppose the scattering of dislocation strain depending on details of mismatch of masses and volumes of atoms in the alloy. The modified scattering due to dislocation strain can be calculated by changing the initial Grüneisen parameter (γ) by adding a change in Grüneisen parameter due to impurity atmosphere (γ_1) (*50*) as given in eqn. 7 (see Table S4).

$$\gamma_1 = \frac{V_{Sb_2Te_3} c_0 K}{k_B T_a} (\gamma \alpha^2 - \alpha \beta) \quad (7)$$

$$\alpha = \frac{(V_{Bi_2Te_3} - V_{Sb_2Te_3})}{V_{Sb_2Te_3}}, \qquad \beta = \frac{1}{2} \frac{(M_{Sb_2Te_3} - M_{Bi_2Te_3})}{M_{Sb_2Te_3}} \quad (8)$$

$V_{Bi_2Te_3}$, $V_{Sb_2Te_3}$, $M_{Bi_2Te_3}$, $M_{Sb_2Te_3}$, K, c_0, T_a are atomic volume of Bi_2Te_3, that of Sb_2Te_3, average atomic mass of Bi_2Te_3, that of Sb_2Te_3, bulk modulus of Sb_2Te_3, concentration of Bi_2Te_3 in $(Bi_{0.25}Sb_{0.75})_2Te_3$ and sample annealing temperature. Since τ_{DS}^{-1} is proportional to γ^2 (see eqn. 6), the reinforcement of scattering of dislocation strain is substantial, increasing τ_{DS}^{-1} by a factor of 2.2.

In addition to the alloy strengthening of τ_{DS}^{-1}, the close proximity of the dislocations compounds the effect. As described by Klemens, when the spacing between dislocations is small, the scattering from the parallel dislocations is reinforced (*10, 45*). If the spacing between dislocations is smaller than phonon wavelength, we should group those dislocations into one dislocation with a new effective Burgers vector (*10, 45, 51*). Since, from a calculation by Wang (*52*), the median wavelength of phonons contributing to lattice thermal conductivity of bismuth telluride is ~ 3.6 nm (wavelength at 50% cumulative thermal conductivity), we can expect a compounding effect for more than half the phonons as the spacing between dislocations is ~ 2.5 nm. Because of the uncertainty of this compounding effect and the actual Burgers vector in all the dislocation arrays, we fit the experimental data with an effective Burgers vector B_D. The effective Burgers vector B_D that fits the experimental data for Te-MS has a magnitude of ~ 12.7 Å, which is

reasonable considering the Burgers vectors (*24*) observed in Bi_2Te_3 and the compounding effect.

Bipolar effects in the total thermal conductivities visible at high temperature of BM, S-MS and Te-MS were estimated by a two band model, which is an extension of a simple parabolic band model (*53*) (the bipolar effect is less than 10% at 300 K for Te-MS). The band structure of the sample was approximated with a conduction band and a valence band. Each band's mass and mobility was determined for different samples by fitting calculated electrical conductivity (σ) and Seebeck coefficient (S) to experimental results of different samples (see Fig. 2A and 2B).

Table S3. Types of scatterings used to calculate the τ_{tot} where τ_U, τ_{PD}, τ_B, $AB_D^2\tau_{DS}$ and τ_{DC} are the phonon relaxation times associated with scatterings from Umklapp processes, point defects, boundaries, dislocation strain and dislocation cores, respectively.

Samples	τ_{tot}^{-1}
BM	$\tau_{tot}^{-1} = \tau_U^{-1} + \tau_{PD}^{-1} + \tau_{B\ (20\ \mu m)}^{-1}$
S-MS	$\tau_{tot}^{-1} = \tau_U^{-1} + \tau_{PD}^{-1} + \tau_{B\ (300\ nm)}^{-1}$
Te-MS	$\tau_{tot}^{-1} = \tau_U^{-1} + \tau_{PD}^{-1} + \tau_{B\ (300\ nm)}^{-1} + AB_D^2\tau_{DS}^{-1} + \tau_{DC}^{-1}$

Table S4. Parameters for the calculation of lattice thermal conductivity

Parameters	Description	Values	Ref.
θ_a	Acoustic mode Debye temperature	94 K	[*42*]
v	Average phonon velocity along *a*-plane	2147 m s^{-1}	[*54*]
v_L	Longitudinal phonon velocity along *a*-plane	2884 m s^{-1}	[*54*]
v_T	Transverse phonon velocity along *a*-plane	1780 m s^{-1}	[*54*]
$\bar{M}$	Average atomic mass of $(Bi_{0.25}Sb_{0.75})_2Te_3$	2.22×10^{-25} kg	-
$M_{Bi_2Te_3}$	Average atomic mass of Bi_2Te_3	2.79×10^{-25} kg	-
$M_{Sb_2Te_3}$	Average atomic mass of Sb_2Te_3	2.07×10^{-25} kg	-
$V_{Bi_2Te_3}$	Atomic volume of Bi_2Te_3	3.40×10^{-29} m^3	-
$V_{Sb_2Te_3}$	Atomic volume of Sb_2Te_3	3.13×10^{-29} m^3	-
V	Average atomic volume of $(Bi_{0.25}Sb_{0.75})_2Te_3$	31.26 $Å^3$	[*9*]
γ	Grüneisen parameter	2.3	[*55*]
r	Poisson's ratio	0.24	[*56*]
N_D	Dislocation density	2×10^{11} cm^{-2}	Exp.
B_D	Magnitude of Burgers vector	12.7 Å	fitted
d	Grain size of BM	20 μm	Exp.
d	Grain size of S-MS and Te-MS	300 nm	Exp.
C_0	Concentration of Bi_2Te_3 in $(Bi_{0.25}Sb_{0.75})_2Te_3$	0.25	-
K	Bulk modulus	44.8 GPa	[*54*]
T_a	Sample annealing temperature	753.15 K	Exp.

Additional Author notes

Author Contributions

S.W.K. and K.H.L. organized the research. S.I.K. and H.A.M fabricated the samples and measured the thermoelectric properties. H.A.M and H.S.K analyzed the data. S.W.K and G.J.S wrote the manuscript. All the authors contributed to the experiments, the analysis of the data and editing of the manuscript.

References

1. L. E. Bell, Cooling, heating, generating power, and recovering waste heat with thermoelectric systems. *Science* **321**, 1457–1461 (2008). Medline doi:10.1126/science.1158899

2. H. Scherrer, S. Scherrer, in *Thermoelectrics Handbook Macro to Nano*, D. M. Rowe, Ed. (CRC, Boca Raton, FL, 2006), chap. 27.

3. R. J. Buist, A simplified method for thermoelectric heat pump optimization. *in 3rd International Conference on Thermoelectric Energy Conversion,* Arlington, Texas, 12 to 14 May 1980 (IEEE, New York, 1980), pp. 130–134.

4. H. J. Goldsmid, in *Electronic Refrigeration* (Pion, London, 1986), chaps. 2 and 7.

5. M. S. Dresselhaus, G. Chen, M. Y. Tang, R. G. Yang, H. Lee, D. Z. Wang, Z. F. Ren, J.-P. Fleurial, P. Gogna, New directions for low-dimensional thermoelectric materials. *Adv. Mater.* **19**, 1043–1053 (2007). doi:10.1002/adma.200600527

6. D. L. Medlin, G. J. Snyder, Interfaces in bulk thermoelectric materials. *Curr. Opin. Colloid Interface Sci.* **14**, 226–235 (2009). doi:10.1016/j.cocis.2009.05.001

7. B. Poudel, Q. Hao, Y. Ma, Y. Lan, A. Minnich, B. Yu, X. Yan, D. Wang, A. Muto, D. Vashaee, X. Chen, J. Liu, M. S. Dresselhaus, G. Chen, Z. Ren, High-thermoelectric performance of nanostructured bismuth antimony telluride bulk alloys. *Science* **320**, 634–638 (2008). Medline doi:10.1126/science.1156446

8. S. Fan, J. Zhao, J. Guo, Q. Yan, J. Ma, H. H. Hng, p-type $Bi_{0.4}Sb_{1.6}Te_3$ nanocomposites with enhanced figure of merit. *Appl. Phys. Lett.* **96**, 182104 (2010). doi:10.1063/1.3427427

9. E. S. Toberer, A. Zevalkink, G. J. Snyder, Phonon engineering through crystal chemistry. *J. Mater. Chem.* **21**, 15843–15852 (2011). doi:10.1039/c1jm11754h

10. P. G. Klemens, The Scattering of Low-Frequency Lattice Waves by Static Imperfections. *Proc. Phys. Soc. A* **68**, 1113–1128 (1955). doi:10.1088/0370-1298/68/12/303

11. P. Kim, L. Shi, A. Majumdar, P. L. McEuen, Thermal transport measurements of individual multiwalled nanotubes. *Phys. Rev. Lett.* **87**, 215502 (2001). Medline doi:10.1103/PhysRevLett.87.215502

12. H. Wang, A. D. LaLonde, Y. Pei, G. J. Snyder, The Criteria for Beneficial Disorder in Thermoelectric Solid Solutions. *Adv. Funct. Mater.* **23**, 1586–1596 (2013). doi:10.1002/adfm.201201576

13. M. Nader, F. Aldinger, M. J. Hoffmann, Influence of the α/β-SiC phase transformation on microstructural development and mechanical properties of liquid phase sintered silicon carbide. *J. Mater. Sci.* **34**, 1197–1204 (1999). doi:10.1023/A:1004552704872

14. P. J. Jorgensen, R. W. Bartlett, Liquid-phase sintering of $SmCo_5$. *J. Appl. Phys.* **44**, 2876–2880 (1973). doi:10.1063/1.1662663

15. S. Nazaré, G. Ondracek, F. Thümmler, in *Relations Between Stereometric Microstructure and Properties of Cermets and Porous Materials* H. H. Hausner, Ed. (Springer, New York, 1971), pp. 171–186.

16. D. Zhao, G. Tan, A review of thermoelectric cooling: Materials, modeling and applications. *Appl. Therm. Eng.* **66**, 15–24 (2014). doi:10.1016/j.applthermaleng.2014.01.074

17. Materials and methods are available as supplementary materials on *Science* Online.

18. D. B. Williams, C. B. Carter, in *Transmission Electron Microscopy* (Springer, New York, 1996).

19. A. Rollett, F. J. Humphreys, G. S. Rohrer, M. Hatherly, in *Recrystallization and related annealing phenomena* (Elsevier, Oxford, ed. 2, 2004).

20. N. Peranio, O. Eibl, Gliding dislocations in Bi_2Te_3 materials. *Phys. Status Solidi A* **206**, 42–49 (2009). doi:10.1002/pssa.200824224

21. R. M. German, P. Suri, S. J. Park, Review: Liquid phase sintering. *J. Mater. Sci.* **44**, 1–39 (2009). doi:10.1007/s10853-008-3008-0

22. C. Herzig, Y. Mishin, in *Diffusion in Condensed Matter* P. Heitjans, J. Kärger, Eds. (Springer, Berlin, Heidelberg, 2005), chap. 8.

23. J. W. Cahn, Y. Mishin, A. Suzuki, Coupling grain boundary motion to shear deformation. *Acta Mater.* **54**, 4953–4975 (2006). doi:10.1016/j.actamat.2006.08.004

24. D. L. Medlin, K. J. Erickson, S. J. Limmer, W. G. Yelton, M. P. Siegal, Dissociated 1/3<0111> dislocations in Bi2Te3 and their relationship to seven-layer Bi3Te4 defects. *J. Mater. Sci.* **49**, 3970–3979 (2014). doi10.1007/s10853-014-8035-4

25. L. P. Hu, T.-J. Zhu, Y.-G. Wang, H.-H. Xie, Z.-J. Xu, X.-B. Zhao, Shifting up the optimum figure of merit of p-type bismuth telluride-based thermoelectric materials for power generation by suppressing intrinsic conduction. *NPG Asia Mater.* **6**, e88 (2014). doi:10.1038/am.2013.86

26. J. Callaway, H. C. von Baeyer, Effect of Point Imperfections on Lattice Thermal Conductivity. *Phys. Rev.* **120**, 1149–1154 (1960). doi:10.1103/PhysRev.120.1149

27. G. A. Slack, S. Galginaitis, Thermal Conductivity and Phonon Scattering by Magnetic Impurities in CdTe. *Phys. Rev.* **133** (1A), A253–A268 (1964). doi:10.1103/PhysRev.133.A253

28. M. Roufosse, P. G. Klemens, Thermal Conductivity of Complex Dielectric Crystals. *Phys. Rev. B* **7**, 5379–5386 (1973). doi:10.1103/PhysRevB.7.5379

29. J. He, S. N. Girard, M. G. Kanatzidis, V. P. Dravid, Microstructure-Lattice Thermal Conductivity Correlation in Nanostructured $PbTe_{0.7}S_{0.3}$ Thermoelectric Materials. *Adv. Funct. Mater.* **20**, 764–772 (2010). doi:10.1002/adfm.200901905

30. B. Abeles, Lattice Thermal Conductivity of Disordered Semiconductor Alloys at High Temperatures. *Phys. Rev.* **131**, 1906–1911 (1963). doi:10.1103/PhysRev.131.1906

31. D. T. Morelli, J. P. Heremans, G. A. Slack, Estimation of the isotope effect on the lattice thermal conductivity of group IV and group III-V semiconductors. *Phys. Rev. B* **66**, 195304 (2002). doi:10.1103/PhysRevB.66.195304

32. D. J. H. Cockayne, I. L. F. Ray, M. J. Whelan, Investigations of dislocation strain fields using weak beams. *Philos. Mag.* **20**, 1265–1270 (1969). doi:10.1080/14786436908228210

33. N. F. Mott, CXVII. A theory of work-hardening of metal crystals. *Philos. Mag.* **43**, 1151–1178 (1952). doi:10.1080/14786441108521024

34. D. R. Clarke, S. R. Phillpot, Thermal barrier coating materials. *Mater. Today* **8**, 22–29 (2005). doi:10.1016/S1369-7021(05)70934-2

35. S. Iwanaga, E. S. Toberer, A. LaLonde, G. J. Snyder, A high temperature apparatus for measurement of the Seebeck coefficient. *Rev. Sci. Instrum.* **82**, 063905 (2011). Medline doi:10.1063/1.3601358

36. K. A. Borup, E. S. Toberer, L. D. Zoltan, G. Nakatsukasa, M. Errico, J. P. Fleurial, B. B. Iversen, G. J. Snyder, Measurement of the electrical resistivity and Hall coefficient at high temperatures. *Rev. Sci. Instrum.* **83**, 123902 (2012). Medline doi:10.1063/1.4770124

37. G. J. Snyder, E. S. Toberer, R. Khanna, W. Seifert, Improved thermoelectric cooling based on the Thomson effect. *Phys. Rev. B* **86**, 045202 (2012). doi:10.1103/PhysRevB.86.045202

38. Y. Liu, Y. Y. Li, S. Rajput, D. Gilks, L. Lari, P. L. Galindo, M. Weinert, V. K. Lazarov, L. Li, Tuning Dirac states by strain in the topological insulator Bi_2Se_3. *Nat. Phys.* **10**, 294–299 (2014). doi:10.1038/nphys2898

39. H. Wang, "International Round-Robin Testing of Bulk Thermoelectrics" (Tech. Rep. ORNL/TM-2011/393, Oak Ridge National Laboratory; High Temperature Materials Laboratory, 2011). doi: 10.2172/1049790

40. G. Min, D. M. Rowe, Cooling performance of integrated thermoelectric microcooler. *Solid-State Electron.* **43**, 923–929 (1999). doi:10.1016/S0038-1101(99)00045-3

41. G. Min, in *Thermoelectrics Handbook: Macro to Nano, Thermoelectric Module Design Theories* (CRC, Boca Raton, FL, 2006).

42. D. Bessas, I. Sergueev, H.-C. Wille, J. Perßon, D. Ebling, R. P. Hermann, Lattice dynamics in Bi_2Te_3 and Sb_2Te_3: Te and Sb density of phonon states. *Phys. Rev. B* **86**, 224301 (2012). doi:10.1103/PhysRevB.86.224301

43. M. Stordeur, H. Sobotta, in *Proc. First European Conf on Thermoelectrics,* D. M. Rowe, Ed. (Pereqrinus Ltd., London, 1988), pp. 209−212.

44. H. J. Goldsmid, A. W. Penn, Boundary scattering of phonons in solid solutions. *Phys. Lett. A* **27**, 523–524 (1968). doi:10.1016/0375-9601(68)90898-0

45. P. G. Klemens, Thermal conductivity and lattice vibrational modes. *Solid State Phys. Adv. Res. Appl.* **7**, 1–98 (1958).

46. P. G. Klemens, in *Thermal Conductivity, vol. 1* R. P. Tye, Ed. (Academic Press, London, 1969), pp. 1−68.

47. J. M. Ziman, in *Electrons and Phonons: The Theory of Transport Phenomena in Solids* (Oxford University Press, 1960).

48. W. R. G. Kemp, P. G. Klemens, R. J. Tainsh, The lattice thermal conductivity of copper alloys: Effect of plastic deformation and annealing. *Philos. Mag.* **4**, 845–857 (1959). doi:10.1080/14786435908238242

49. J. N. Lomer, H. M. Rosenberg, The detection of dislocations by low temperature heat conductivity measurements. *Philos. Mag.* **4**, 467–483 (1959). doi:10.1080/14786435908233416

50. A. J. Friedman, T. K. Chu, P. G. Klemens, C. A. Reynolds, Lattice Thermal Conductivity of a Neutron-Irradiated Copper-Aluminum Alloy. *Phys. Rev. B* **6**, 356–363 (1972). doi:10.1103/PhysRevB.6.356

51. N. F. Mott, CXVII. A theory of work-hardening of metal crystals. *Philos. Mag.* **43**, 1151–1178 (1952). doi:10.1080/14786441108521024

52. Y. Wang, B. Qiu, A. J. H. McGaughey, X. Ruan, X. Xu, Mode-wise thermal conductivity of bismuth telluride. *J. Heat Transfer* **135**, 091102 (2013). doi: 10.1115/1.4024356

53. A. F. May, E. S. Toberer, A. Saramat, G. J. Snyder, Characterization and analysis of thermoelectric transport in n-type $Ba_8Ga_{16-x}Ge_{30+x}$. *Phys. Rev. B* **80**, 125205 (2009). doi:10.1103/PhysRevB.80.125205

54. F. Yang, T. Ikeda, G. J. Snyder, C. Dames, Effective thermal conductivity of polycrystalline materials with randomly oriented superlattice grains. *J. Appl. Phys.* **108**, 034310 (2010). doi:10.1063/1.3457334

55. X. Chen, H. D. Zhou, A. Kiswandhi, I. Miotkowski, Y. P. Chen, P. A. Sharma, A. L. Lima Sharma, M. A. Hekmaty, D. Smirnov, Z. Jiang, Thermal expansion coefficients of Bi_2Se_3 and Sb_2Te_3 crystals from 10 K to 270 K. *Appl. Phys. Lett.* **99**, 261912 (2011). doi:10.1063/1.3672198

56. H. H. Landolt, R. Börnstein, in *Numerical Data and Functional Relationships in Science and Technology*, vol. 17f (Springer, Berlin, 1983), pp. 272–278.